Structural Defects of Silver Hollandite, $Ag_xMn_8O_y$, Nanorods: Dramatic Impact on Electrochemistry

Lijun Wu,[†] Feng Xu,[†,‡] Yimei Zhu,[*,†] Alexander B. Brady,[⊥] Jianping Huang,[§] Jessica L. Durham,[§] Eric Dooryhee,[∥] Amy C. Marschilok,[§,⊥] Esther S. Takeuchi,[§,⊥,#] and Kenneth J. Takeuchi[*,§,⊥]

[†]Condensed Matter Physics and Materials Science Department, Brookhaven National Laboratory, Upton, New York 11973, United States, [‡]SEU-FEI Nano-Pico Center, Key Laboratory of MEMS of the Ministry of Education, School of Electronic Science and Engineering, Southeast University, Nanjing, 210096, PR China, [§]Department of Chemistry, Stony Brook University, Stony Brook, New York 11794, United States, [⊥]Department of Materials Science and Engineering, Stony Brook University, Stony Brook, New York 11794, United States, [∥]Photon Science Division, National Synchrotron Light Source II, Brookhaven National Laboratory, Upton, New York 11973, United States, and [#]Energy Sciences Directorate, Brookhaven National Laboratory, Upton, New York 11973, United States

ABSTRACT Hollandites (OMS-2) are an intriguing class of sorbents, catalysts, and energy storage materials with a tunnel structure permitting one-dimensional insertion and deinsertion of ions and small molecules along the *c* direction. A 7-fold increase in delivered capacity for $Li/Ag_xMn_8O_{16}$ electrochemical cells (160 *versus* 23 mAh/g) observed upon a seemingly small change in silver content ($x \sim 1.1$ (L-Ag-OMS-2) and 1.6 (H-Ag-OMS-2)) led us to characterize the structure and defects of the silver hollandite material. Herein, Ag hollandite nanorods are studied through the combined use of local (atomic imaging, electron diffraction, electron energy-loss spectroscopy) and bulk (synchrotron based X-ray diffraction, thermogravimetric analysis) techniques. Selected area diffraction and high resolution transmission electron microscopy show a structure consistent with that refined by XRD; however, the Ag occupancy varies significantly even within neighboring channels. Both local and bulk measurements indicate a greater quantity of oxygen vacancies in L-Ag-OMS-2, resulting in lower average Mn valence relative to H-Ag-OMS-2. Electron energy loss spectroscopy shows a lower Mn oxidation state on the surface relative to the interior of the nanorods, where the average Mn valence is approximately $Mn^{3.7+}$ for H-Ag-OMS-2 and $Mn^{3.5+}$ for L-Ag-OMS-2 nanorods, respectively. The higher delivered capacity of L-Ag-OMS-2 may be related to more oxygen vacancies compared to H-Ag-OMS-2. Thus, the oxygen vacancies and MnO_6 octahedra distortion are assumed to open the MnO_6 octahedra walls, facilitating Li diffusion in the *ab* plane. These results indicate crystallite size and surface defects are significant factors affecting battery performance.

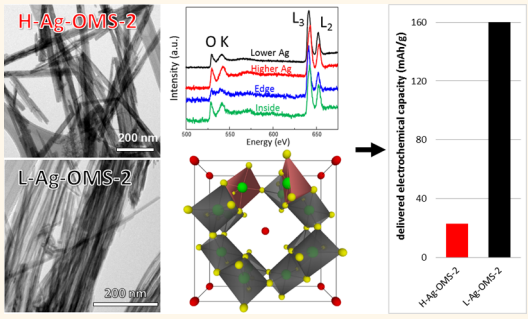

KEYWORDS: silver hollandite · octahedral molecular sieve · oxygen defects · transmission electron microscopy · electron energy loss spectroscopy · lithium battery

Hollandites (often termed octahedral molecular sieves, OMS-2) are an intriguing class of manganese oxides with a tunnel structure that provides a robust framework for insertion and deinsertion of ions and small molecules. This structure has allowed them to function as sorbents and catalysts under a variety of applications.[1−6] Specifically, hollandite type materials consist of octahedral units of edge-sharing manganese oxide octahedra (MnO_6) which interlink to form tunnels of 2×2 (0.46 nm) dimensions.[7] Bimetallic hollandite type materials have been prepared where cations with 1+ or 2+ charge partially occupy locations within the manganese oxide tunnels, and the Mn cations possess mixed 3+ and 4+ oxidation states.[8,9] Typically, the ion located within the tunnel is inert; however, silver hollandite is an interesting case as the Ag^+ cationic center is potentially electrochemically active.

Although reports involving synthesis of hollandite structured materials are abundant,[7,10−12] the preparation of pure silver hollandite has remained elusive. The synthesis of silver hollandite was first described in 1984 *via* a high temperature, high pressure

* Address correspondence to zhu@bnl.gov, kenneth.takeuchi.1@stonybrook.edu.

Received for review May 31, 2015 and accepted July 16, 2015.

Published online July 16, 2015
10.1021/acsnano.5b03274

solid-state route.[13,14] Notably, the unit cell of silver hollandite could accommodate two silvers per formula unit, resulting in a formula of $Ag_2Mn_8O_{16}$; however, the single crystal structure showed silver hollandite to have a formula of $Ag_{1.8}Mn_8O_{16}$ indicating a 89.7% tunnel occupancy.[13] Hydrothermal syntheses of silver hollandite were reported in 2007[15] and in 2011,[16] utilizing silver permanganate ($AgMnO_4$) and manganese nitrate ($Mn(NO_3)_2$) as reagents. A reflux based synthesis for preparation of silver hollandite was described in 2007,[15] which incorporated a high temperature calcination step which resulted in the presence of a pyrolusite (β-MnO_2) impurity. More recently, we reported a reflux preparation including the ability to tune the material properties of silver hollandite ($Ag_xMn_8O_{16}$) *via* modifications in the reflux synthesis conditions.[17,18] With a change in Ag to Mn ratios, we observed a concomitant variance in crystallite size and associated particle size and bulk surface area, demonstrating ability to synthetically control the material properties.

The ability to prepare pure silver hollandite in sufficient quantity enabled the first electrochemical assessment.[17] Further, the synthetic control enabling systematic variation of physical properties facilitated a more detailed exploration of the electrochemical behavior of silver hollandite.[18] Electrochemical testing was conducted for a series of silver hollandite, $Ag_xMn_8O_{16}\cdot nH_2O$, samples over a range of silver (x) content, ranging from $1.0 \leq x \leq 1.8$, $n \sim 2$. Constant current discharge, pulse testing, galvanostatic intermittent titration type (GITT) testing and cycle testing each demonstrated improved performance of the smaller crystallite size materials with improved reversibility and delivered capacity as a result of crystallite size/silver content reduction.[19] The results affirm the opportunity to improve electrochemical performance of active electrode materials by tuning the material properties *via* appropriate design of the synthesis method. The signature channel-like hollandite structure with a general formula of $A^{II}[M^{IV}, M^{III}]_8O_{16}$ might give rise to unexpected exotic properties. For instance, a new class of multiferroic hollandite $BaMn_3Ti_4O_{14.25}$ was recently synthesized. Structural characterization including electron microscopy revealed that it contains Mn^{4+} and Mn^{3+} and exhibits correlated antiferromagnetic and ferroelectric order.[20] One-dimensional $ZnMn_2O_4$ nanowires exhibited high power capability at elevated current rates, attributed to enhanced kinetics of the nanowire electrode.[21]

Fundamental studies involving the impact of physical and chemical properties of materials on their electrochemical properties are critical to the rational development of battery materials which may address the present and future requirements for stationary and portable power. Thus, the combined use of synchrotron based diffraction, thermogravimetric analysis, atomic imaging, nanodiffraction and electron energy-loss spectroscopy, as reported here, permits bulk and local measurement of structure, silver content, oxygen content, and the associated manganese oxide coordination environment. This work shows that structural defects can have a significant and even dominant desirable effect on material battery function, illustrated here by differences in electrochemical capacity.

RESULTS AND DISCUSSION

Silver hollandite samples, $Ag_xMn_8O_{16}\cdot nH_2O$, n = 0.7−0.9, were selected for this study with compositions of low silver content, x = 1.16−1.22 (L-Ag-OMS-2) and high silver content, x = 1.60−1.65 (H-Ag-OMS-2). The variation in silver occupancy from synthesis to synthesis was minor. For eight samples prepared under the H-Ag-OMS-2 condition, the mean and standard deviation, respectively, for the silver (x) content were 1.60 and 0.03. For 19 samples prepared under the L-Ag-OMS-2 condition, the mean and standard deviation, respectively, for the silver (x) content were 1.14 and 0.04. Our results were consistent with prior literature, where it was noted that it is difficult to maintain a complete anhydrous material for hollandite type structures, *i.e.*, α-MnO_2.[22] While the samples in this study contained 0.8 H_2O per formula unit on average, for simplicity, we do not list the water content for each sample. The theoretical capacity for the $Ag_{1.20}Mn_8O_{16}$ (L-Ag-OMS-2) material is 260 mAh/g while that of $Ag_{1.60}Mn_8O_{16}$ (H-Ag-OMS-2) is 247 mAh/g with only a ∼5% difference in capacity expected. However, under 35 mA/g discharge, the x = 1.2 sample delivered 160 mAh/g (402 mWh/g) while the sample with x = 1.6 delivered 23 mAh/g (61 mWh/g) to 2.0 V; thus, nearly 7 fold increase in delivered capacity was observed, Figure S1. The significant difference in delivered capacity cannot be rationalized by differences in composition alone motivating more detailed study of silver hollandite nanorods.

This is the first report of Rietveld refinement of silver hollandite nanowires using synchrotron X-ray diffraction data, Figure 1, Table 1. The high signal-to-background ratio of the synchrotron diffraction provides the needed sensitivity and accuracy to find lattice parameters and atomic factors with a high degree of accuracy for a nanocrystalline material. The silver hollandite structure was first reported by Jansen, for $Ag_{1.8}Mn_8O_{16}$. Jansen performed single crystal diffraction on material produced though a high temperature and pressure synthesis, and found that silver hollandite fit an *I*4/*m* space group to very high accuracy.[13] Subsequent studies have used powder diffraction data and relied on Jansen's structure.[18] In keeping with previous literature, we have also used Jansen's *I*4/*m* structure. The Rietveld refinement of the silver hollandite nanorod powders is difficult due to significant crystal shape anisotropy of the samples. In this case, goodness of fit values (R_{wp} and R_{exp})

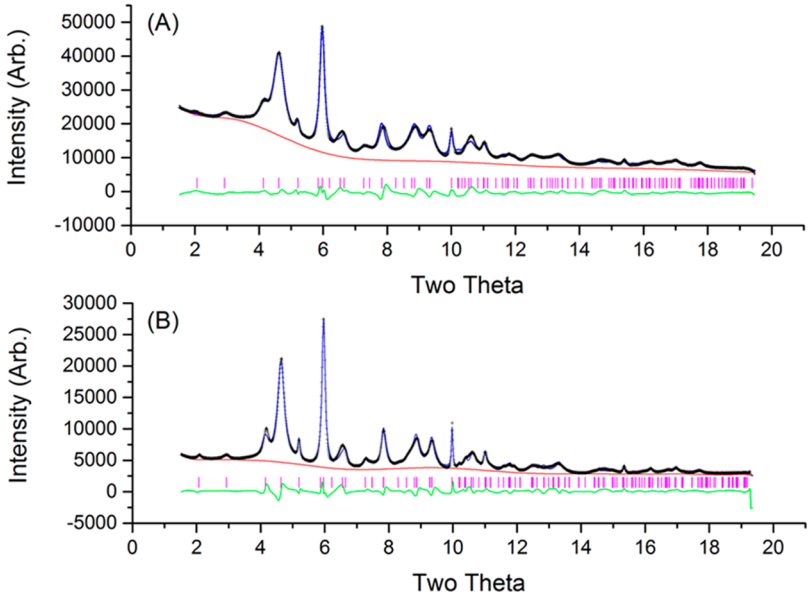

Figure 1. Synchrotron X-ray diffraction data and Rietveld refinement of a) $Ag_{1.22}Mn_8O_{16}$ (L-Ag-OMS-2) and b) $Ag_{1.66}Mn_8O_{16}$ (H-Ag-OMS-2).

TABLE 1. Structural Parameters from Rietveld Refinement for $Ag_{1.22}Mn_8O_{16}$ (L-Ag-OMS-2) and $Ag_{1.66}Mn_8O_{16}$ (H-Ag-OMS-2)[a]

chemical composition		$Ag_{1.22}Mn_8O_{16}$	$Ag_{1.66}Mn_8O_{16}$
unit cell	a	9.770(2)	9.738(2)
	b	9.770(2)	9.738(2)
	c	2.8536(3)	2.8620(2)
space group		*I*4/*m*	*I*4/*m*
data points		1888	1887
contributing reflections		210	210
R_{wp}		3.23%	5.03%
R_{exp}		2.49%	3.81%

[a] R_{wp} is the weighted coefficient of determination for the fitting. The weights are based on assumed errors (0.01%) in the data set. R_{exp} is the best possible fit that can be achieved if the assumed errors are correct, as discussed in ref 36.

range from 2.5 to 5.0%, as detailed in Table 1. R_{wp} is the weighted coefficient of determination for the fitting. The weights are based on assumed errors (0.01%) in the data set. R_{exp} is the best possible fit that can be achieved if the assumed errors are correct.

Both material samples are consistent with the silver hollandite structure, with no discernible crystalline impurities. Select bond distances and angles from the Rietveld refinement of the silver hollandite nanowire samples are shown in Table S1. The high silver H-Ag-OMS-2 material shows less angular distortion in the MnO_6 octahedral structure (average O−Mn−O angle deviation from 90°) but more Mn−O bond-length variation, consistent with the higher crystallinity of the high silver material. The L-Ag-OMS-2 sample shows a larger value of 9.770 for the *a* and *b* dimension compared to 9.738 Å for the high silver sample, H-Ag-OMS-2, Table 1. Prior studies on hollandite manganese oxide tunnel structures have shown that Group I metal cations (including K^+ and Na^+) increase the dimensions of the 2 × 2 tunnels where higher occupancies of the tunnel ions increase the lattice parameters.[23] The refined structures from the data collected on the silver hollandite samples were used to calculate the tunnel dimensions in the *ab* plane bisecting the silver sites. In contrast to the results reported for the Group I metal cations, our results for silver ions show that higher occupancy of silver decreases the *a* and *b* lattice parameters. The silver hollandite structure prepared at high temperature with a silver content of $x = 1.8$ has a tunnel dimension of 4.873 Å in the *ab* plane bisecting the silver from the analysis of a single crystal.[13] As the silver content decreases to $x = 1.66$ (H-Ag-OMS-2) and 1.22 (L-Ag-OMS-2), the tunnel dimensions increase to 5.072 and 5.176 Å, respectively. Thus, the trend observed at all three silver levels indicates decreased lattice parameters with increasing silver content likely related to more covalent bonding character of the silver ion compared to Group I metal ions.

Additionally, the Rietveld refinements for the silver hollandite materials indicate strongly anisotropic crystallite sizes where the crystallite size in the *c*-direction is at least 200 nm for both samples. The crystallite widths (in the *a* and *b* direction) are all short, ranging from 8 nm for L-Ag-OMS-2 to 10 nm for H-Ag-OMS-2. Crystallite sizes estimated from the Rietveld refinement were consistent with the TEM observations, as discussed below. The magnitude of the thermal displacement parameters for silver along the *c*-axis for our L-Ag-OMS-2 and H-Ag-OMS-2 materials was consistent with Jansen's single crystal observations for $Ag_{1.8}Mn_8O_{16}$.[13]

The silver hollandite samples were examined *via* transmission electron microscopy (TEM) and were confirmed to have a nanorod shape, Figure 2(a,b).

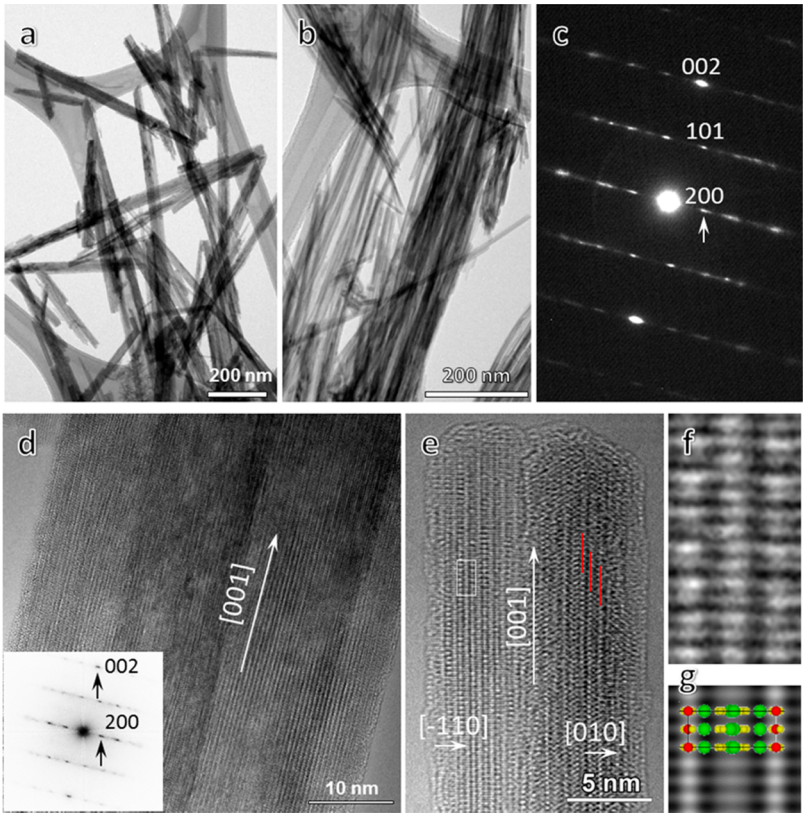

Figure 2. Morphology and structure of Hollandite nanorods. (a,b) Typical TEM bright field images from (a) $Ag_{1.63}Mn_8O_{16}$ (H-Ag-OMS-2) and (b) $Ag_{1.16}Mn_8O_{16}$ (L-Ag-OMS-2). The diameter of the nanorods is about 40−50 nm and 10−15 nm for H-Ag-OMS-2 and L-Ag-OMS-2, respectively. The length of the nanorods can be a few micrometers. (c,d) Electron diffraction pattern (EDP) (c) and HRTEM image (d) from a H-Ag-OMS-2 nanorod. Both EDP and diffractogram of the HRTEM image (inset in (d)) show the (010)* zone of the body-centered tetragonal Hollandite, consistent with the structure determined by XRD. The long axis of the nanorod is along [001] direction. (e) HRTEM image of an L-Ag-OMS-2 nanorod. The nanorod consists of two grains with left one orientated along [110] and right one on [100]. (f) Magnified image from the marked area in (e). (g) Simulated image based on the structure model in Takeuchi *et al.*[18] The [110] projection of the structure with red, green and yellow spheres representing Ag, Mn and O is also included. Although the simulated image overall agrees with the observation, the image intensity variations in the experimental image suggest that there are vacancies on Ag site and distortion of MnO_6 octahedra.

Representative TEM bright field images for higher Ag content (H-Ag-OMS-2) $Ag_{1.63}Mn_8O_{16}$, Figure 2a, and lower silver content (L-Ag-OMS-2) $Ag_{1.16}Mn_8O_{16}$, Figure 2b, show the diameters of the nanorods ranging from 20 to 50 nm for H-Ag-OMS-2 hollandite, while from a few nanometers up to 20 nm for L-Ag-OMS-2 hollandite. The length of the nanorods for both H-Ag-OMS-2 and L-Ag-OMS-2 materials can be several micrometers long. High resolution TEM (HRTEM) images were recorded for the samples, Figure 2(d,e), and show that the nanorods consist of several crystalline grains (or subrods) which are highly anisotropic. The lengths are as long while the diameters are a few nanometers for L-Ag-OMS-2 and a larger 10−20 nm for H-Ag-OMS-2 hollandite nanorods. Both the electron diffraction pattern (EDP, Figure 2c) from the nanorod, as well as the diffractogram from the HRTEM (inset in Figure 2d) can be indexed as the (010)* zone of the body-centered tetragonal hollandite, consistent with the structure determined by XRD.[18] The long axis of the nanorod is along the [001] direction. Further we noted that the Bragg spots elongate along the [100]* direction. By tilting the nanorods to different orientations, we found that the diffraction spots always elongate along the direction which is perpendicular to the [001]* direction, indicating that the spots have the disk-shape with its normal axis along the [001]* direction. The disk-shape of the diffraction spots can be attributed to the shape effect of the nanorods as well as the defects. Figure 2(e) shows a HRTEM image of a L-Ag-OMS-2 nanorod, which consists of two crystalline grains with the image on the left side orientated along [110], and the image on the right side along [100] direction. Overall, the image on the left appears structurally well ordered. However, a close inspection, as shown in the magnified image in Figure 2(f), shows considerable intensity variations in both Ag and MnO columns, in contrast to the uniform intensity distribution in Ag and MnO columns in the simulated image, Figure 2(g), calculated based on the perfect crystal structure, indicating the existence of point defects in the nanorod. The right grain in Figure 2(e) is quite disordered. Stacking faults along the [010] direction are present, as indicated by the red lines.

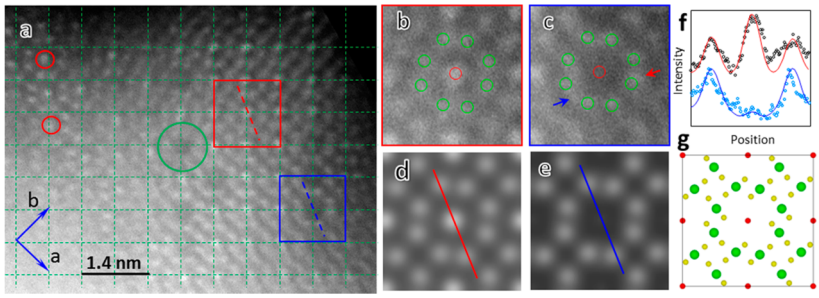

Figure 3. (a) STEM high angle dark field (HAADF) image from $Ag_{1.63}Mn_8O_{16}$ (H-Ag-OMS-2) viewed along [001] direction. The local displacement of unit cell is clearly visible, as indicated by reference green grid and red circles. The occupancy of Ag in the middle of the channel varies a lot. (b,c) Magnified images from the area marked by red and blue squares, showing different Ag occupancy. The projected positions of Ag (red circle) and surrounding 8 Mn (green circles) from XRD refined structure model are embedded in (b) and (c). The blue arrow in (c) marks the extra intensity peak between two Mn columns. The red arrow points out the deviated Mn column position, indicating local distortion of MnO_6 octahedra. (d,e) Calculated STEM-HAADF images of $Ag_xMn_8O_{16}$ with (d) $x = 1.6$ and (e) $x = 0.5$, respectively. They match with the observations in (b) and (c) very well. (f) Intensity profiles. The black and blue circles are from the red and blue dash scan lines in (a). The solid red and blue lines are from the scan lines in (d) and (e). (g) [001] projection of the XRD refined structure model. The red, green and yellow spheres represent Ag, Mn and O, respectively.

The defect structures in the silver hollandite nanorods can be better understood by high resolution scanning transmission electron microscopy (STEM) with a high angle annular dark field (HAADF) detector, as its contrast is proportional to $Z^{1.7}$ along the atom column, where Z is the atomic number. Figure 3(a) shows a STEM-HAADF image from a H-Ag-OMS-2 nanorod viewed along the [001] direction with collection angle from 67 to 275 mrad. Although the sample is very thick along this direction, the basic hollandite structure is clearly resolved, as shown in the magnified image in Figure 3(b) where Ag and eight surrounding Mn are clearly seen and are consistent with the [001] projection of the structure refined by XRD. Oxygen is invisible in the STEM-HAADF image due to its weak scattering power (low Z). Various lattice distortions are present, as indicated by the red circles which deviate from the periodic position (cross of the dash lines). The image intensity at the Ag column varies significantly; *e.g.*, the one marked by the red-square is very strong, while that marked by the blue-square is very weak. This indicates significant variation of Ag occupancy.

To quantify the occupancy of the Ag, we generated a series of calculated STEM-HAADF images with different Ag occupancies. Figure 3(d,e) shows Ag content at $x = 1.6$ and $x = 0.5$ in $Ag_xMn_8O_{16}$, which agree with the experiments in Figure 3(b) and Figure 3(c), respectively. Quantitative comparison is shown in the plots in Figure 3(f). From a series of comparisons between the observations and image calculations, we conclude that the Ag content varies from 0.4 to 1.8 locally within the H-Ag-OMS-2 material. In addition to the image intensity variation at Ag site, image intensity at Mn site changes as well. Moreover, Mn columns in some areas, as indicated by the green circle (Mn atoms are inside the circle) in Figure 3(a) and arrows in Figure 3(c), become diffuse and the corresponding image intensities are weak, indicating distortion of the MnO_6 octahedra.

The occupancy variation at Ag and the distortion of MnO_6 can be also seen when the nanorods are viewed along the [110] direction. Figure 4(a) shows STEM-HAADF image for a L-Ag-OMS-2 nanorod viewed along the [110] direction. The thickness of the nanorod along the beam direction decreases from left to right. In a relatively thick area (left side in Figure 4a), the image intensity is averaged over many atoms through the thickness. Comparing to the image calculated based on the perfect structure model (Figure 4d), they agree well, indicating the structure of the nanorod overall is consistent with the Ag hollandite structure. In the very thin area (right side in Figure 4a), there are fewer atoms over the thickness and therefore, the defects are more easily seen. In Figure 4c, deviations of the Mn atoms from the projected positions of the perfect structure model are clearly visible, as indicated by the vertical lines in Figure 4c, indicating the significant distortion of the MnO_6 octahedra.

As functional properties of the material may be strongly affected by oxygen vacancies, ion valences and surface structures of the electrode materials were more closely examined. By using electron energy loss spectroscopy (EELS), in particular the spectral imaging in the STEM mode, we are able to measure the oxygen vacancies and the Mn valence state in Ag hollandite nanorods. Figure 5(a) shows the typical EELS spectra for O K edge and Mn L_3, L_2 edges from the L-Ag-OMS-2 (black line) and H-Ag-OMS-2 (red line) nanorods after zero-loss calibration, background subtraction and multiple scattering correction. The spectra are normalized with the Mn L_3 edge. The intensity of the O K edge in L-Ag-OMS-2 nanorod is lower than that in H-Ag-OMS-2 nanorod, indicating greater quantities of O vacancies in the L-Ag-OMS-2 nanorod. The ratios of O to Mn calculated based on dozens of EELS measurements are 1.85 and 1.95 for the L-Ag-OMS-2 and H-Ag-OMS-2 nanorods, respectively, where the same intensity

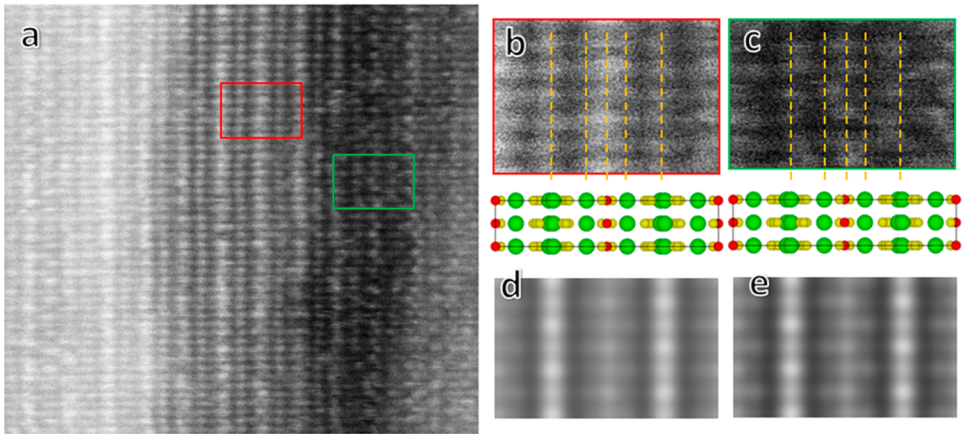

Figure 4. (a) STEM-HAADF image for $Ag_{1.16}Mn_8O_{16}$ (L-Ag-OMS-2) viewed along [110] direction. (b,c) magnified images from (b) the red and (c) the green rectangle area in (a). The [110] projection of the XRD refined structure model is shown in the bottom. The vertical lines are guide lines for observing deviations of Mn atoms. (d,e) Images calculated based on the XRD refined structure model at thickness of (d) 10 nm and (e) 5 nm, respectively.

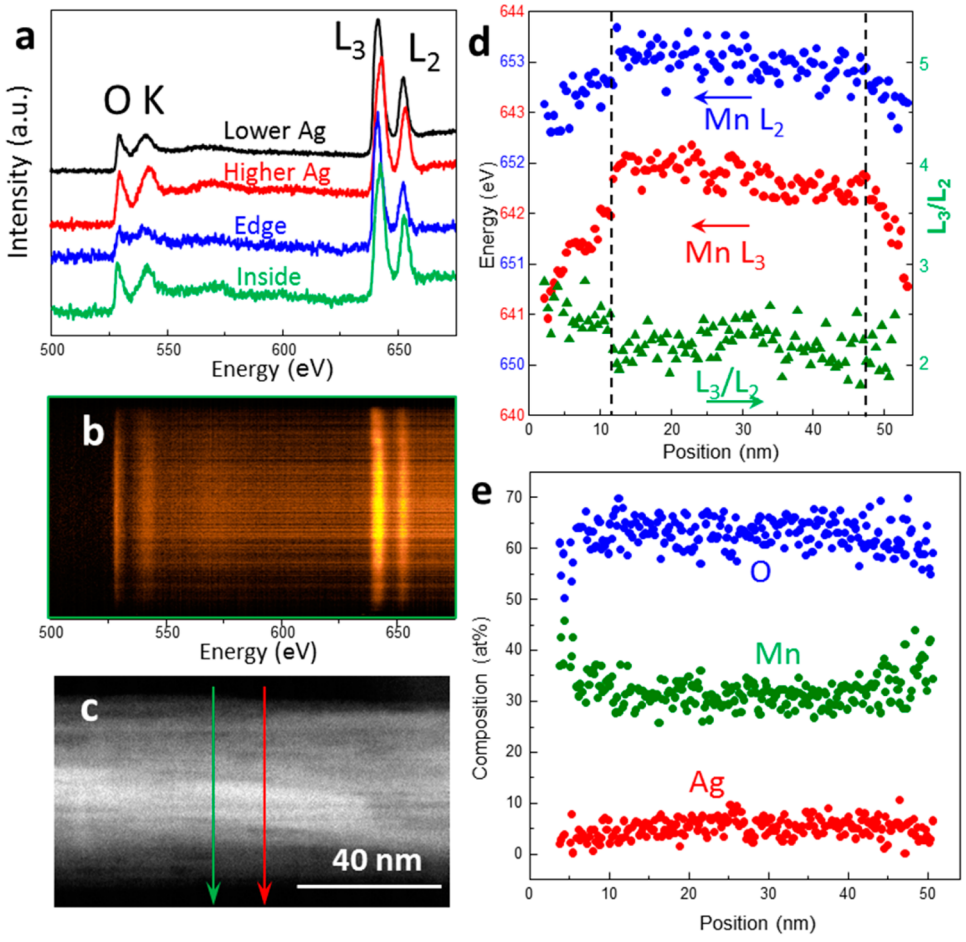

Figure 5. (a) EELS from lower ($Ag_{1.16}Mn_8O_{16}$, L-Ag-OMS-2, black) and higher ($Ag_{1.63}Mn_8O_{16}$, H-Ag-OMS-2, red) Ag content samples, as well as edge (blue) and interior (green) of an nanorod of H-Ag-OMS-2 sample. The spectra are normalized with the Mn L_3 edge having the same intensity for comparison. (b) EELS spectrum image with energy dispersion of 0.1 eV/channel from the vertical green line in a H-Ag-OMS-2 nanorod shown in (c). (c) STEM-HAADF image of a H-Ag-OMS-2 nanorod. (d) Energies of Mn L_3 (red) and L_2 (blue) refined from the spectrum image in (b). The intensity ratio of L_3/L_2 is also included (green). (e) Relative composition map calculated from another EELS spectrum image with lower energy dispersion (0.25 eV/channel) from the vertical red scan line shown in (c).

normalization and energy window were used for each sample to achieve an accurate comparison. The energies of the L_3 and L_2 edges in L-Ag-OMS-2 nanorod are lower than those in H-Ag-OMS-2 nanorod.

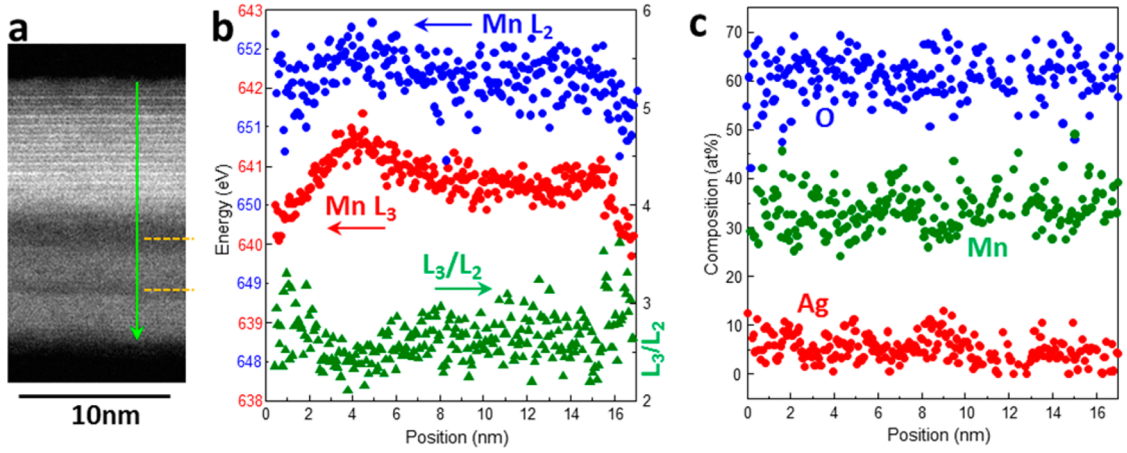

Figure 6. (a) STEM-HAADF image from a $Ag_{1.16}Mn_8O_{16}$ (L-Ag-OMS-2) nanorod which consists of three subrods. The diameter of the top subrod is about 8 nm, while that of bottom two subrods is about 4.5 nm. The horizontal orange dash lines mark the boundaries of three subrods. The green arrow is the scan line for EELS spectrum image. (b) Energies of Mn L_3 (red) and L_2 (blue) edges, as well as intensity ratio of L_3/L_2 (green) from the EELS spectrum image. (c) Relative composition map from the EELS spectrum image.

Moreover, the intensity ratio of L_3/L_2 in the L-Ag-OMS-2 nanorod is higher than that in H-Ag-OMS-2 nanorod, indicating that the valence of Mn in L-Ag-OMS-2 nanorod is lower than that in H-Ag-OMS-2 nanorod. The average Mn L_3/L_2 intensity ratios measured based on Pearson method are about 2.2 for H-Ag-OMS-2 and 2.45 for L-Ag-OMS-2, respectively.[24] The Ag in the Ag hollandite is expected to donate electrons, thus reducing the valence of Mn. The Mn valence in the L-Ag-OMS-2 nanorod should therefore have higher valence in comparison with the H-Ag-OMS-2 nanorod. More oxygen vacancies in the L-Ag-OMS-2 nanorod, however, would reduce Mn valence. When considering both the differences in Ag occupancy and the presence of oxygen vacancies, the average Mn valence can be estimated to be about $Mn^{3.7+}$ for H-Ag-OMS-2 and $Mn^{3.5+}$ for L-Ag-OMS-2 nanorods, respectively. Therefore, the reduced Mn valence in L-Ag-OMS-2 nanorod can be attributed to more oxygen vacancies in the nanorod.

The distribution of the composition and valence state across the nanorod was measured using EELS spectrum imaging across the nanorod. Figure 5(b) is an EELS spectrum image from a vertical green scan line in a H-Ag-OMS-2 nanorod of Figure 5(c), showing O K, Mn L_3 and L_2 edges. The Mn L_3 and L_2 edges are quite straight inside the nanorod, but shift to lower energy at both edges of the rod, indicating the reduced valence of Mn on the surface. The difference between the surface (edges of the rod) and inside of the rod can be clearly seen in the spectra shown in Figure 5(a). The energy of the Mn L_3 and L_2 edges from the surface (blue line) is lower than that from the inside of the rod. The intensity ratio of the L_3/L_2 is also higher for the surface, indicating the reduction of Mn valence. It is also seen that the intensity of O K edge is lower on the surface, indicating more oxygen vacancies on the surface. Figure 5(d) plots the energies of Mn L_3 and L_2 edges, as well as their intensity ratio of L_3/L_2, as a function of the position measured from the spectrum image in Figure 5(b). The reduced Mn L_3 and L_2 energies, as well as the increased L_3/L_2 intensity ratio, are clearly observed on both surfaces (edges) of the nanorod, confirming the reduced Mn valence. The average L_3/L_2 intensity ratio inside the nanorod, *e.g.*, between two vertical dash lines in Figure 5(d), is about 2.2, while that on the surface (outside of dash lines) is about 2.5. The corresponding Mn valence can be estimated to be about 3.7^+ and 3.1^+ for the interior and the surface of the nanorod, respectively. Figure 5(e) plots the relative composition of Ag, Mn and O calculated from an EELS spectrum image which has lower energy dispersion to include the Ag M edge. The distributions of Ag, Mn and O are quite uniform inside the nanorod, except on the surface where there are less O and Ag. The reduced Mn valence state on the surface can be therefore partially attributed to the O vacancies on the surface.

We performed similar EELS analysis for the L-Ag-OMS-2 nanorods, as shown in Figure 6. The nanorod consists of three subrods with the diameter of about 8 nm for the top one and 4.5 nm for the bottom two subrods. Similar to the H-Ag-OMS-2 nanorod, the energies of the Mn L_3 and L_2 edges inside the top subrod are higher than that at the edge, while their intensity ratio L_3/L_2 is lower (Figure 6b), indicating the reduced Mn valence on the surface. Interestingly, the energies of the Mn L_3 and L_2 edges in the bottom two subrods are lower than those inside the top subrod, while the L_3/L_2 intensity ratio is higher, indicating the overall Mn valence in the bottom two subrods is lower than that in the top one. We attribute this to the surface effect because the size of the bottom two subrods is very small, just half the size of the top one. Unlike the H-Ag-OMS-2 nanorod, the composition distributions of Ag, Mn and O in this L-Ag-OMS-2 nanorod look uniform

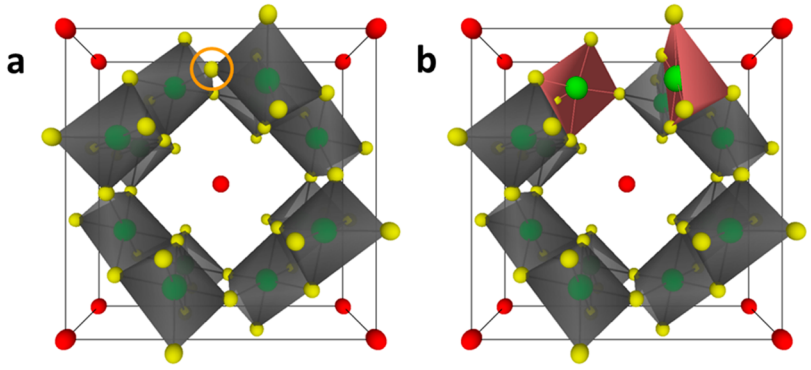

Figure 7. (a) Perspective view of hollandite ($Ag_2Mn_8O_{16}$) along [001] direction. Ag is surrounded by eight MnO_6 octahedra, forming a tunnel which extends along the [001] direction. (b) An oxygen marked by orange circle in (a) is removed. The MnO_6 octahedra wall is therefore broken, facilitating Li ion diffusion in the *ab* plane.

although the overall O content is low in comparison with H-Ag-OMS-2 nanorod.

Thermogravimetric analysis (TGA) was employed to monitor thermal decomposition and assess the water and oxygen content of bulk silver hollandite samples with silver contents of $x = 1.16$ (L-Ag-OMS-2) and 1.60 (H-Ag-OMS-2) under a nitrogen atmosphere. The TGA experimental details were adapted from previous thermal investigation of hollandite-type structures.[15,25−27] Dehydration of water adsorbed on the surface of hollandite and water within the tunneled MnO_6 motif is observed below 360 °C, Figure S2a, consistent with an average water content of 0.8 H_2O per $Ag_xMn_8O_y$ formula unit and a range of $n = 0.7-0.9$ for the $Ag_xMn_8O_y \cdot nH_2O$ samples.

Decomposition of silver hollandite, $Ag_xMn_8O_{16}$ between 360 and 750 °C occurs *via* a succession of weight-loss events that include a breakdown of the MnO_6 tunneled structure, the formation of silver metal and Mn_2O_3, and the decomposition of Mn_2O_3 into Mn_3O_4, in the reducing nitrogen atmosphere, eq 1.[26,28] The decomposition of low silver content hollandite ($x = 1.16$, L-Ag-OMS-2) occurs at lower temperatures than the high silver content hollandite ($x = 1.60$, H-Ag-OMS-2), indicating lower intrinsic thermal stability for the L-Ag-OMS-2 material, Figure S2a. Analysis of the postdecomposition TGA samples *via* XRD confirms the exclusive presence of silver metal and Mn_3O_4, Figure S2b. During decomposition, the weight loss corresponds to the evolution of O_2 which can be used to systematically assess the oxygen content of silver hollandite samples with distinct compositions. The weight-loss profile and the first derivative as a function of temperature were used to determine the precise region of oxygen loss for the calculation, Figure S2a. The calculated oxygen contents of 14.8 ($x = 1.16$, L-Ag-OMS-2) and 15.7 ($x = 1.60$, H-Ag-OMS-2) by the TGA method yield compositions of $Ag_{1.16}Mn_8O_{14.8}$ and $Ag_{1.60}Mn_8O_{15.7}$. Thus, the TGA bulk results for determination of oxygen vacancy are consistent with the results of TEM elemental analysis by EELS which provided local compositions of $Ag_{1.16}Mn_8O_{14.8}$ and $Ag_{1.63}Mn_8O_{15.6}$ for the L-Ag-OMS-2 and H-Ag-OMS-2 materials, respectively.

$$\begin{aligned} Ag_xMn_8O_{16} \cdot nH_2O &\rightarrow Ag_xMn_8O_{16} \\ &\rightarrow xAg + 4Mn_2O_3 + 2O_2 \\ &\rightarrow xAg + 8/3Mn_3O_4 + 8/3O_2 \end{aligned} \quad (1)$$

CONCLUSIONS

In summary, silver hollandite, $Ag_xMn_8O_{16} \cdot nH_2O$, $n = 0.8$, with low silver content, ($x = 1.12-1.16$, L-Ag-OMS-2) exhibited a 7 fold increase in discharge capacity in lithium based batteries relative to the high silver content material ($x = 1.60-1.66$, H-Ag-OMS-2). Oxygen vacancies are the most common type of defect for hollandite manganese oxides, and such vacancies can play an important role in controlling catalytic activity as well as conductivity.[29] We demonstrate here that the presence of surface defects through oxygen vacancy may play a significant role in electrochemistry as well. Bulk and local measurements indicate higher quantities of oxygen vacancies for L-Ag-OMS-2. The significance of the oxygen vacancies can be best understood through consideration of the crystallographic structure of silver hollandite. Silver hollandite has a body-centered tetragonal structure where the Ag is surrounded by eight MnO_6 octahedra, forming a tunnel with a dimension of ~0.51 nm in the *ab* plane which extends along the [001] direction, Figure 7. Though there is a small gap (less than 0.06 nm) in the *a* or *b* direction, in the *ab* plane all directions are basically closed by MnO_6 octahedra. Therefore, if the nanorod has no defects, the diffusion of Li ions in *ab* plane would be limited. The oxygen vacancies and MnO_6 octahedra distortion may open the MnO_6 octahedra walls, facilitating Li ion diffusion in the *ab* plane. Thus, the higher capacity of the L-Ag-OMS-2 samples may be due to not only to the smaller crystallite size but also to the presence of more oxygen vacancies as compared to the H-Ag-OMS-2 samples. From an oxidation state perspective, the L-Ag-OMS-2

nanorods with lower Mn valence would be expected to show lower capacity during discharge based on average oxidation state and difference in formula weight. However, the opposite effect is observed where the deliverable capacity of the L-Ag-OMS-2 nanorods is substantially higher than that of the H-Ag-OMS-2 samples. Thus, the impact of small crystallite size and surface defects, specifically oxygen vacancies, appear to be significant in determining the electrochemical performance.

EXPERIMENTAL METHODS

Silver hollandite was prepared using an ambient pressure reflux reaction approach as previously described.[17,18] After synthesis, samples were annealed at 300 °C for 6 h. Briefly, silver permanganate ($AgMnO_4$), nitric acid (HNO_3), and manganese sulfate monohydrate ($MnSO_4 \cdot H_2O$) were used for the synthesis and their ratios were varied to control silver content in the products. The Ag/Mn ratio in the silver hollandite product samples was determined using inductively coupled plasma spectrometry-optical emission spectroscopy (ICP-OES) with a Thermofisher iCAP 6300 series instrument. A TA Instruments SDT Q600 was used to collect simultaneous thermogravimetric analysis/differential scanning calorimetry (TGA/DSC) for investigation of the thermal stability and oxygen content of silver hollandite samples. TGA was conducted in alumina thermogravimetric analysis pans and heated from room temperature to 950 °C under an atmosphere of nitrogen gas at a rate of 1 °C/min. X-ray diffraction (XRD) data were collected at room temperature using a Rigaku Smart Lab system (Cu Kα radiation) with Bragg−Brentano configuration. Patterns of all as-prepared samples were indexed to $Ag_{1.8}Mn_8O_{16}$,[30] while patterns of post-TGA samples were indexed to Mn_3O_4 (ICSD 31094) and Ag metal (ICSD 64706).

High-resolution TEM/STEM imaging, electron diffraction, chemical and Mn valence mapping were performed using the double aberration-corrected JEOL-ARM200CF microscope with a cold-field emission gun and operated at 200 kV. The microscope is equipped with JEOL and Gatan HAADF detectors for incoherent HAADF (Z-contrast) imaging, Gatan GIF Quantum ER Energy Filter with dualEELS for EELS. The energy positions of Mn L_3 and L_2 were obtained by fitting the EELS spectrum with a combined Gaussian and Lorentz function. The L_3/L_2 intensity ratio was calculated from the EELS spectrum based on Pearson method with double step functions.[31] To assist interpretation of the HRTEM and HRSTEM images, image simulations were carried out using our own computer codes based on the multislice method with frozen phonon approximation.[32]

X-ray powder diffraction (XPD) was performed on L-Ag-OMS-2 and H-Ag-OMS-2 samples where x = 1.22 and 1.66 silver, respectively. Ceria powder was used as a standard. The samples were sealed in capillaries and positioned in the synchrotron X-ray beam at the XPD 1 beamline in NSLS-II. The beam was calibrated to a wavelength of 0.2478 Å. Detection was performed using a 16-in. amorphous silicon digital flat panel fitted with a CsI scintillator. During measurements the sample was rotated to reduce preferred orientation effects. The two-dimensional data was integrated to simulate a one-dimensional pattern using the Fit2D software.[33]

Rietveld refinement was carried out using GSAS II.[34] Instrumental parameters were fit using a ceria standard. Each powder pattern was first fit using the LeBail-Pawley method[35] to find particle and microstrain broadening. Then the broadening parameters were fixed while the atomic structure parameters were fit using the standard Rietveld method. As a final step, all parameters were included in the refinement.

For electrochemical analysis, a mixture of silver hollandite, graphite, super P carbon black and polyvinylidene fluoride (PVDF) was used as the cathode. Coin cells were assembled using the cathode, Li foil, polypropylene separators, and the electrolyte (1 M $LiPF_6$ in ethylene carbonate/dimethyl carbonate at a volume ratio of 30:70). Discharge testing was done at 30 °C under a 35 mA/g constant current.

Conflict of Interest: The authors declare no competing financial interest.

Acknowledgment. This work was supported as part of the Center for Mesoscale Transport Properties, an Energy Frontier Research Center supported by the U.S. Department of Energy, Office of Science, Basic Energy Sciences, under award #DE-SC0012673. TEM work was supported by the U.S. Department of Energy, Office of Basic Energy Science, Division of Materials Science and Engineering, under Contract No. DE-SC0012704. Use of the National Synchrotron Light Source II, Brookhaven National Laboratory, was supported by the U.S. Department of Energy, Office of Science, Office of Basic Energy Sciences, under Contract No. DE-SC0012704. The authors express their appreciation to Milinda Abeykoon and Jianming Bai for helpful discussions related to X-ray powder diffraction refinement.

Supporting Information Available: **Table S1.** Parameters from Rietveld refinement for (A) $Ag_{1.22}Mn_8O_{16}$ (L-Ag-OMS-2) and (B) $Ag_{1.66}Mn_8O_{16}$ (H-Ag-OMS-2). (i) Wyckoff positions and (ii) Mn−O distances and angles. Debye−Waller factors are shown as Biso values. **Figure S1.** Discharge of Li/$Ag_{1.20}Mn_8O_{16}$ (L-Ag-OMS-2) and Li/$Ag_{1.60}Mn_8O_{16}$ (H-Ag-OMS-2) cells under a constant current of 35 mA/g. **Figure S2.** (a) Thermogravimetric analysis (TGA) and first derivative of weight as a function of temperature for $Ag_{1.16}Mn_8O_{16}$ (L-Ag-OMS-2, gray) and $Ag_{1.60}Mn_8O_{16}$ (H-Ag-OMS-2, black) (b) Post-TGA X-ray diffraction pattern of silver hollandite with Mn_3O_4 (ICSD 31094, blue) and Ag metal (ICSD 64706, red) reference patterns. The Supporting Information is available free of charge on the ACS Publications website at DOI: 10.1021/acsnano.5b03274.

REFERENCES AND NOTES

1. Nicolas-Tolentino, E.; Tian, Z.-R.; Zhou, H.; Xia, G.; Suib, S. L. Effects of Cu2+ Ions on the Structure and Reactivity of Todorokite- and Cryptomelane-Type Manganese Oxide Octahedral Molecular Sieves. *Chem. Mater.* **1999**, *11*, 1733–1741.
2. Tsuji, M.; Komarneni, S. Selective Exchange of Divalent Transition Metal Ions in Cryptomelane-Type Manganic Acid with Tunnel Structure. *J. Mater. Res.* **1993**, *8*, 611–616.
3. Li, L.; King, D. L. Synthesis and Characterization of Silver Hollandite and Its Application in Emission Control. *Chem. Mater.* **2005**, *17*, 4335–4343.
4. Dyer, A.; Pillinger, M.; Newton, J.; Harjula, R.; Möller, T.; Amin, S. Sorption Behavior of Radionuclides on Crystalline Synthetic Tunnel Manganese Oxides. *Chem. Mater.* **2000**, *12*, 3798–3804.
5. Dharmarathna, S.; King'ondu, C. K.; Pedrick, W.; Pahalagedara, L.; Suib, S. L. Direct Sonochemical Synthesis of Manganese Octahedral Molecular Sieve (OMS-2) Nanomaterials Using Cosolvent Systems, Their Characterization, and Catalytic Applications. *Chem. Mater.* **2012**, *24*, 705–712.
6. Huang, H.; Sithambaram, S.; Chen, C.-H.; King'ondu Kithongo, C.; Xu, L.; Iyer, A.; Garces, H. F.; Suib, S. L. Microwave-Assisted Hydrothermal Synthesis of Cryptomelane-Type Octahedral Molecular Sieves (OMS-2) and Their Catalytic Studies. *Chem. Mater.* **2010**, *22*, 3664–3669.
7. Ching, S.; Suib, S. L. Synthetic Routes to Microporous Maganese Oxides. *Comments Inorg. Chem.* **1997**, *19*, 263–282.
8. Vicat, J.; Fanchon, E.; Strobel, P.; Duc Tran, Q. The Structure of K1.33Mn8O16 and Cation Ordering in Hollandite-Type Structures. *Acta Crystallogr., Sect. B: Struct. Sci.* **1986**, *B42*, 162–167.
9. Ozawa, T.; Suzuki, I.; Sato, H. Structural, Magnetic, and Electronic Transport Properties of Novel Hollandite-Type

Molybdenum Oxide, Rb1.5Mo8O16. *J. Phys. Soc. Jpn.* **2006**, *75*, 014802−1–014802−8.
10. Li, W.-N.; Crisostomo, V. M. B.; Nyutu, E. K.; Ding, Y.-S.; Suib, S. L. Transitional Metal Oxide (TMO) Nanorods: Synthesis, Characterization, Properties and Applications. *Nanorods, Nanotubes Nanomater. Res. Prog.* **2008**, 203–238.
11. Suib, S. L.; O'Young, C.-L. Synthesis of Octahedral Molecular Sieves and Layered Materials. *Chem. Ind. (Boca Raton, FL, U. S.)* **1997**, *69*, 215–231.
12. Brock, S. L.; Duan, N.; Tian, Z. R.; Giraldo, O.; Zhou, H.; Suib, S. L. A Review of Porous Manganese Oxide Materials. *Chem. Mater.* **1998**, *10*, 2619–2628.
13. Chang, F. M.; Jansen, M. Ag1.8Mn8O16: Square planar coordinated Ag+ ions in the channels of a novel hollandite variant. *Angew. Chem., Int. Ed. Engl.* **1984**, *23*, 906–907.
14. Chang, F. M.; Jansen, M. The First Silver Hollandite. *Rev. Chim. Miner.* **1986**, *23*, 48–54.
15. Chen, J.; Tang, X.; Liu, J.; Zhan, E.; Li, J.; Huang, X.; Shen, W. Synthesis and Characterization of Ag-hollandite Nanofibers and its Catalytic Application in Ethanol Oxidation. *Chem. Mater.* **2007**, *19*, 4292–4299.
16. Sun, Y.; Hu, X.; Zhang, W.; Yuan, L.; Huang, Y. Large-Scale Synthesis of $Ag_{1.8}Mn_8O_{16}$ Nanorods and their Electrochemical Lithium-Storage Properties. *J. Nanopart. Res.* **2011**, *13*, 3139–3148.
17. Zhu, S.; Marschilok, A. C.; Lee, C.-Y.; Takeuchi, E. S.; Takeuchi, K. J. Synthesis and Electrochemistry of Silver Hollandite. *Electrochem. Solid-State Lett.* **2010**, *13*, A98–A100.
18. Takeuchi, K. J.; Yau, S. L. Z.; Menard, M. C.; Marschilok, A. C.; Takeuchi, E. S. Synthetic Control of Composition and Crystallite Size of Silver Hollandite, AgxMn8O16: Impact on Electrochemistry. *ACS Appl. Mater. Interfaces* **2012**, *4*, 5547–5554.
19. Takeuchi, K. J.; Yau, S. Z.; Subramanian, A.; Marschilok, A. C.; Takeuchi, E. S. The Electrochemistry of Silver Hollandite Nanorods, AgxMn8O16: Enhancement of Electrochemical Battery Performance *via* Dimensional and Compositional Control. *J. Electrochem. Soc.* **2013**, *160*, A3090–A3094.
20. Liu, S.; Akbashev, A. R.; Yang, X.; Liu, X.; Li, W.; Zhao, L.; Li, X.; Couzis, A.; Han, M.-G.; Zhu, Y. Hollandites as a New Class of Multiferroics. *Sci. Rep.* **2014**, *4*, 6203.
21. Kim, S.-W.; Lee, H.-W.; Muralidharan, P.; Seo, D.-H.; Yoon, W.-S.; Kim, D.; Kang, K. Electrochemical performance and *ex situ* analysis of ZnMn2O4 nanowires as anode materials for lithium rechargeable batteries. *Nano Res.* **2011**, *4*, 505–510.
22. Shao-Horn, Y.; Hackney, S. A.; Johnson, C. S.; Thackeray, M. M. Microstructural Features of α - MnO2 Electrodes for Lithium Batteries. *J. Electrochem. Soc.* **1998**, *145*, 582–589.
23. Gao, T.; Norby, P. Frame Stability of Tunnel-Structured Cryptomelane Nanofibers: The Role of Tunnel Cations. *Eur. J. Inorg. Chem.* **2013**, *2013*, 4948–4957.
24. Riedl, T.; Gemming, T.; Wetzig, K. Extraction of EELS White-Line Intensities of Manganese Compounds: Methods, Accuracy, and Valence Sensitivity. *Ultramicroscopy* **2006**, *106*, 284–291.
25. Feng, Q.; Kanoh, H.; Miyai, Y.; Ooi, K. Alkali Metal Ions Insertion/Extraction Reactions with Hollandite-Type Manganese Oxide in the Aqueous Phase. *Chem. Mater.* **1995**, *7*, 148–153.
26. Tanaka, Y.; Tsuji, M.; Tamaura, Y. ESCA and Thermodynamic Studies of Alkali Metal Ion Exchange Reactions on an α-MnO_2 Phase with the Tunnel Structure. *Phys. Chem. Chem. Phys.* **2000**, *2*, 1473–1479.
27. Huang, H.; Meng, Y.; Labonte, A.; Dobley, A.; Suib, S. L. Large-Scale Synthesis of Silver Manganese Oxide Nanofibers and Their Oxygen Reduction Properties. *J. Phys. Chem. C* **2013**, *117*, 25352–25359.
28. Chen, J.; Tang, X.; Liu, J.; Zhan, E.; Li, J.; Huang, X.; Shen, W. Synthesis and Characterization of Ag-Hollandite Nanofibers and Its Catalytic Application in Ethanol Oxidation. *Chem. Mater.* **2007**, *19*, 4292–4299.
29. Suib, S. L. Structure, Porosity, and Redox in Porous Manganese Oxide Octahedral Layer and Molecular Sieve Materials. *J. Mater. Chem.* **2008**, *18*, 1623–1631.
30. Chang, F. M.; Jansen, M. $Ag_{1.8}Mn_8O_{16}$: square planar coordinated Ag+ ions in the channels of a novel hollandite variant. *Angew. Chem., Int. Ed. Engl.* **1984**, *23*, 906–907.
31. Pearson, D. H.; Ahn, C. C.; Fultz, B. White Lines and d-Electron Occupancies for the 3d and 4d Transition Metals. *Phys. Rev. B: Condens. Matter Mater. Phys.* **1993**, *47*, 8471–8478.
32. Kirkland, E. J. *Advanced Computing in Electron Microscopy*; Plenum: New York, 1998.
33. Hammersley, A. P.; Svensson, S. O.; Hanfland, M.; Fitch, A. N.; Häusermann, D. Two-Dimensional Detector Software: From Real Detector to Idealised Image or Two-Theta Scan. *High Pressure Res.* **1996**, *14*, 235–248.
34. Toby, B. H.; Von Dreele, R. B. GSAS-II: The Genesis of a Modern Open-Source all purpose Crystallography Software Package. *J. Appl. Crystallogr.* **2013**, *46*, 544–549.
35. Pawley, G. Unit-Cell Refinement from Powder Diffraction Scans. *J. Appl. Crystallogr.* **1981**, *14*, 357–361.
36. Toby, B.H. R Factors in Rietveld Analysis: How Good Is Good Enough? *Powder Diffr.* **2006**, *21*, 67.